SCIENCE CHINA
Physics, Mechanics & Astronomy

•Article•

September 2021 Vol. 64 No. 9: 297011
https://doi.org/10.1007/s11433-021-1727-6

Dimensional crossover tuned by pressure in layered magnetic $NiPS_3$

Xiaoli Ma[1†], Yimeng Wang[2†], Yunyu Yin[1†], Binbin Yue[3], Jianhong Dai[1], Jinguang Cheng[1,4], Jianting Ji[1], Feng Jin[1], Fang Hong[1,4,5*], Jian-Tao Wang[1,4,5*], Qingming Zhang[6,1*], and Xiaohui Yu[1,4,5*]

[1] *Beijing National Laboratory for Condensed Matter Physics, Institute of Physics, Chinese Academy of Sciences, Beijing 100190, China;*
[2] *Department of Physics, Renmin University of China, Beijing 100872, China;*
[3] *Center for High Pressure Science and Technology Advanced Research, Beijing 100094, China;*
[4] *School of Physical Sciences, University of Chinese Academy of Sciences, Beijing 100049, China;*
[5] *Songshan Lake Materials Laboratory, Dongguan 523808, China;*
[6] *School of Physical Science and Technology, Lanzhou University, Lanzhou 730000, China*

Received February 10, 2021; accepted May 28, 2021; published online August 3, 2021

The physical properties of most 2D materials are highly dependent on the nature of their interlayer interaction. In-depth studies of the interlayer interaction are beneficial to the understanding of the physical properties of 2D materials and permit the development of related devices. Layered magnetic $NiPS_3$ has unique magnetic and electronic properties. The electronic band structure and corresponding magnetic state of $NiPS_3$ are expected to be sensitive to the interlayer interaction, which can be tuned by external pressure. Here, we report an insulator-metal transition accompanied by the collapse of magnetic order during the 2D-3D structural crossover induced by hydrostatic pressure. A two-stage phase transition from a monoclinic ($C2/m$) to a trigonal ($P\bar{3}1m$) lattice is identified via *ab initio* simulations and confirmed via high-pressure X-ray diffraction and Raman scattering; this transition corresponds to a layer-by-layer slip mechanism along the *a*-axis. Temperature-dependent resistance measurements and room temperature infrared spectroscopy under different pressures demonstrate that the insulator-metal transition and the collapse of the magnetic order occur at ~20 GPa, which is confirmed by low-temperature Raman scattering measurements and theoretical calculations. These results establish a strong correlation between the structural change, electric transport, and magnetic phase transition and expand our understanding of layered magnetic materials. Moreover, the structural transition caused by the interlayer displacement has significance for designing similar devices at ambient pressure.

metal-insulator transition, magnetic phase transition, structural phase transition

PACS number(s): 71.30.+h, 75.30.Kz, 68.18.Fg

Citation: X. Ma, Y. Wang, Y. Yin, B. Yue, J. Dai, J. Cheng, J. Ji, F. Jin, F. Hong, J.-T. Wang, Q. Zhang, and X. Yu, Dimensional crossover tuned by pressure in layered magnetic $NiPS_3$, Sci. China-Phys. Mech. Astron. **64**, 297011 (2021), https://doi.org/10.1007/s11433-021-1727-6

*Corresponding authors (Fang Hong, email: hongfang@iphy.ac.cn; Jian-Tao Wang, email: wjt@aphy.iphy.ac.cn; Qingming Zhang, email: qmzhang@ruc.edu.cn; Xiaohui Yu, email: yuxh@iphy.ac.cn)
†These authors contributed equally to this work.

1 Introduction

In most condensed matter systems, dimensionality plays an important role in determining the structural, electronic, and magnetic properties. Layered materials with van der Waals (vdW) interactions provide a good platform for examining how the phases and interactions evolve when the material is tuned from the 2D limit to the 3D state. Since graphene was first stripped from natural graphite by Andre Geim and Konstantin Novoselov [1], a large number of 2D materials with atomic thickness have emerged and attracted the attention of the scientific community. One class of such a material is the 2D transition metal dichalcogenides [2-4]. Recently, layered transition metal trichalcogenides (MPX_3; M = Fe, Ni, or Mn; X = S or Se) in an antiferromagnetic (AFM) state [5-13] have attracted considerable attention because of their tunable electronic properties and potential applications as magnetic materials and spintronic devices [14,15]. These compounds are joined by vdW interactions and thus bring together both magnetism and correlated electron physics with vdW materials [16-19].

MPX_3 compounds are typical 2D AFM materials. The axial distortion of the MX_6 octahedron may produce an anisotropy that can dominate the spin dimension (Ising, XY, or Heisenberg model). For example, $FePS_3$ is described by the Ising model, $NiPS_3$ conforms to the XY model, and $MnPS_3$ can be described using the Heisenberg model [6,9,20]. The magnetic exchange of these compounds is dominated by the superexchange interaction, and the sign and properties of the superexchange interaction depend on the M-S-M angle of the metal ion and the electron occupancy rate. Certain MPX_3 materials exhibit more than one magnetic phase transition with changes in temperature. It is therefore of great significance to extend the use of these MPX_3 materials to the field of spintronics.

In addition to magnetism, MPX_3 compounds also have rich electronic properties. Many materials are Mott or charge-transfer insulators with a wide range of electronic bandgaps ranging from 0.25 to 3.5 eV [19,21-27]. These bandgaps can be tuned by changing relevant parameters. For example, monolayer MoS_2 changes from a direct-bandgap to an indirect-bandgap semiconductor under high pressure, whereas MoS_2 in bulk form undergoes a metallic transition under high pressure [28]. Furthermore, many research groups have conducted high-pressure studies on MPX_3 and reported or predicted an insulator-metal transition [29-36].

With the rapid development of 2D materials, pressure has become an important parameter to tune the states of materials and examine their fundamental physical properties. Such properties that can be tuned include structural phase transitions, electronic behavior, and even magnetism. For example, at sufficient pressure, the bandgap of many materials will close, and the material will exhibit an insulator-metal transition. Many novel and rich physical properties can be obtained through pressure regulation. MPX_3 provides an ideal case study to investigate how phases and interactions evolve when the system is tuned from the 2D limit to the 3D state through pressure.

In this study, we report a systematic study on the structure, electronic properties, and magnetism of $NiPS_3$ under pressure. A two-stage phase transition with a 2D-3D crossover is reported in bulk $NiPS_3$ via *ab initio* calculations, high-pressure X-ray diffraction (XRD), and Raman scattering measurements. During the structural phase transition, the interlayer distance changes more evidently compared with other unit cell parameters. The first structural phase transition occurs at a pressure of ~15 GPa, and the new structure belongs to the same space group ($C2/m$) as the ambient structure with an $a/3$ slip along the a-axis. Furthermore, the magnetic-order collapse and insulator-metal transition in pressurized bulk $NiPS_3$ are observed at a pressure of ~20 GPa through high-pressure resistance, infrared, and Raman scattering measurements. The second structural phase transition occurs at ~27 GPa with an $a/2$ slip along the a-axis, and its space group becomes $P\bar{3}1m$; here, the material exhibits 3D behavior.

2 Materials and methods

2.1 Sample synthesis

Single crystals of $NiPS_3$ were grown using the chemical vapor transport (CVT) method. The crystal naturally cleaves along the [001] surface, forming $NiPS_3$ flakes weakly bonded by vdW forces. High-purity nickel, phosphorus, and sulfur elements were mixed in a stoichiometric mole ratio of 1:1:3 (around 1 g in total), and iodine (about 0.123 g) was used as a transport agent. These raw materials were sealed into a quartz ampoule with a length of ~16 cm and an external diameter (D) of 13 mm, and the pressure inside the quartz ampoule was pumped down to 1×10^{-4} Torr. The quartz ampoule was then placed into a two-zone furnace (680°C-720°C) and heated for two weeks. The quartz ampoule was then cooled to room temperature, and bulk crystals were obtained from the top of the quartz ampoule.

2.2 High-pressure measurements

High-pressure four-probe electrical resistance, XRD, and Raman scattering measurements were performed in diamond anvil cells (DACs). DACs composed of BeCu alloy with two opposing anvils were used to generate high pressure. Diamond anvils with 300 μm culets were used for measurements. In these experiments, a thin single crystal sample with dimensions of 10 μm × 50 μm × 100 μm was loaded into the sample chamber (D = 120 μm hole) in a rhenium gasket with

a c-BN insulating layer, and a ruby ball was loaded to serve as the internal pressure standard. The ruby fluorescence method was used to determine the pressure. The high-pressure four-probe electrical resistance measurements were performed at high-pressure synergetic measurement station of synergetic extreme condition user facility [37].

The high-pressure XRD measurements were performed at beamline 4W2 of the Beijing Synchrotron Radiation Facility. A monochromatic X-ray beam with a wavelength of 0.6199 Å was used for the measurements. Silicone oil was used as the pressure-transmitting medium.

The high-pressure and temperature-dependent Raman spectra were collected using an HR800 spectrometer (Jobin Yvon) equipped with a liquid-nitrogen-cooled charge-coupled device (CCD) and volume Bragg gratings, for which a micro-Raman backscattering configuration was adopted. A 633 nm laser was used, with a spot size of 5 μm focused on the sample surface. The laser power was maintained at ~1.4 mW to avoid overheating during the measurements. KBr was used as the pressure-transmitting medium.

The high-pressure infrared experiments were performed at room temperature using a Bruker VERTEX 70v infrared spectroscopy system with a HYPERION 2000 microscope. A thick $NiPS_3$ single crystal was used, and KBr was used as the pressure-transmitting medium. The spectra were collected in transmission and reflection modes in the range of 600-8000 cm^{-1}, with a resolution of 4 cm^{-1} through a ~30 μm × 30 μm aperture.

2.3 Computational methods

The calculations presented here were performed using the Vienna *ab initio* simulation package (VASP) [38] with the projector augmented wave method [39] and the spin polarized generalized gradient approximation [40] for the exchange-correlation energy. The valence states of $3d^9 4s^1$ for Ni, $3s^2 3p^3$ for P, and $3s^2 3p^4$ for S were used with the energy cutoff of 550 eV for the plane wave basis set. To simulate the interlayer interaction, a 1 × 1 × 2 supercell (in AA stacking including 8 $NiPS_3$ formula) was used with a vdW correction [41]. An intralayer zigzag AFM structure [42] was set with the interlayer ferromagnetic coupling. The Brillouin zone was sampled with a 7 × 4 × 4 Monkhorst-Pack special k-point grid. Throughout our calculations with or without pressure, the convergence criteria employed for both the electronic self-consistent relaxation and the ionic relaxation were set to 10^{-6} eV and 0.01 eV/A for energy and force, respectively.

Following the reconstruction mechanism of graphite, Si, and Ge reported by Wang et al. [43,44], in our simulations, to determine the high-pressure structure, we manually manipulate the sliding and connecting patterns between the layers via a one-layer by one-layer slip mechanism along the in-plane *a*,*b*-axis (see Figure 1(d)). According to the one-layer by one-layer slip mechanism under pressure, various possible structures are obtained. We then relax each structure via *ab initio* calculations and compare the simulated XRD pat-

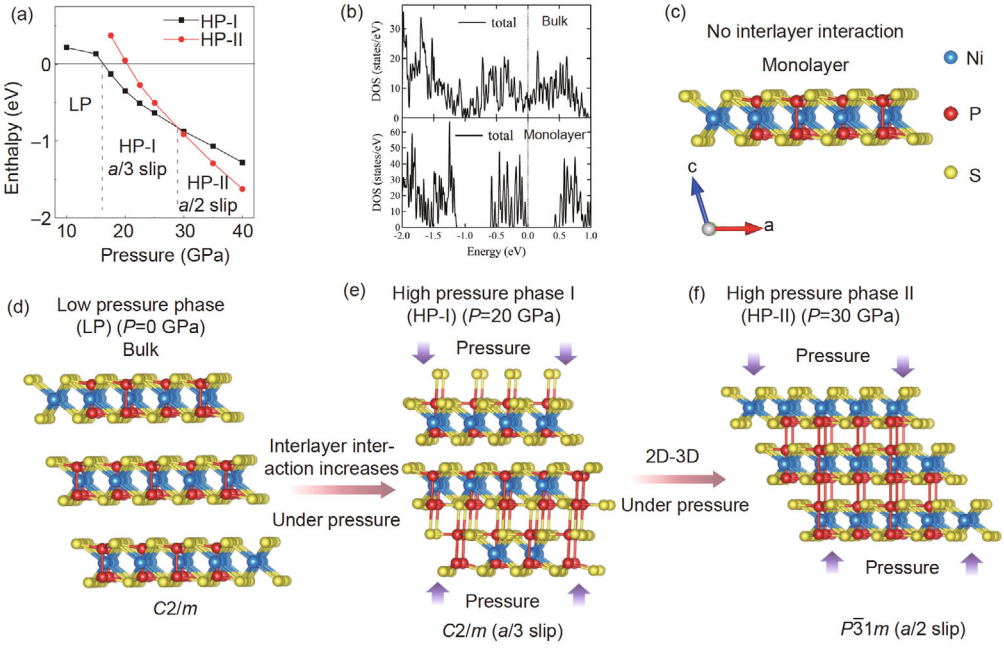

Figure 1 (Color online) Scheme of the $NiPS_3$ structure evolution under high pressure. (a) Enthalpy of the HP-I and HP-II phases relative to the LP phase under varying pressure; (b) total electronic DOS for bulk and monolayer $NiPS_3$ at 20 GPa; (c) structure for monolayer $NiPS_3$; (d) LP structure of $NiPS_3$ with the *C*2/*m* space group (view along the *b*-axis); (e) HP-I structure for $NiPS_3$ with the *C*2/*m* space group, which slides by *a*/3 along the *a*-axis relative to the LP phase; (f) HP-II structure for $NiPS_3$ with the $P\bar{3}1m$ space group, which slides by *a*/2 along the *a*-axis relative to the LP phase. The Ni, P, and S atoms are shown in blue, red, and yellow, respectively.

terns with the experimental XRD data. The *a*/3 slip structure is more stable than the other structures in the range of 16-28 GPa; the *a*/2 slip structure is more stable >28 GPa (see Figure 1(a)); the calculated XRD patterns for both these phases are in good agreement with the experimental XRD patterns (see Figure S1). This indicates that the phases obtained in this work can be determined via a layer-by-layer slip mechanism along the *a*-axis.

Our simulations based on the layer-by-layer slip mechanism allow us to understand the phase transition mechanism and determine the high-pressure structure of the layered system. Basing on the layer-by-layer sliding and connecting mechanism, we have recently successfully predicted a new high-pressure network structure of β-$EuSn_2As_2$ phase with *C*2/*m* symmetry [45].

3 Results and discussion

3.1 Structural phase transition

At ambient conditions, $NiPS_3$ has a layered structure with monoclinic (*C*2/*m*, No. 12) symmetry [21,46]. To explore the structural changes of $NiPS_3$ under pressure, we performed a detailed *ab initio* simulation using a double cell along the *c*-axis (Figure 1(d)), and we reported a phase transition pathway via the layer-by-layer slip mechanism along the *a*-axis. Compared with monolayer $NiPS_3$ without interlayer interaction (Figure 1(c)), the structure of bulk $NiPS_3$ with interlayer interactions significantly changes under pressure (Figure 1(d)-(f)). Figure 1(a) shows the enthalpy change of the different phases under pressure relative to the original monoclinic phase. According to the principle of the lowest energy, we confirm three phases up to 40 GPa. We temporarily define the structure at 0 GPa as the low-pressure (LP) phase; the phase at 20 GPa is defined as the high-pressure I (HP-I) phase; finally, the phase at 30 GPa is defined as the high-pressure II (HP-II) phase. The LP phase is reported to exist at <16 GPa, the HP-II phase is favorable at >28 GPa, and the HP-I phase is observed in the range of 16-28 GPa. The HP-I phase is thus reported to be an intermediate state. Figure 1(d) shows the crystal structure of the LP phase of $NiPS_3$. Viewed along the *b*-axis, we can see the well-separated sandwich layers associated with the weak interlayer vdW interaction. The HP-I structure exhibits an *a*/3 slip along the *a*-axis (Figure 1(e)). The slip between the *ab* planes with pressure is feasible as the planes are only weakly bound by the vdW forces, and the layers can therefore slide easily over one another. The LP and HP-I phases are separated by an isostructural phase transition; they belong to the same space group *C*2/*m*. The HP-II structure has an *a*/2 slip along the *a*-axis (Figure 1(f)). This phase transition leads to the closely related $P\bar{3}1m$ (No. 162) trigonal structure, which adopts a higher symmetry in the paramagnetic (PM) state. From the LP to the HP-II phase, we can clearly see a 2D-3D crossover via the intermediate state of the HP-I phase. These results suggest a two-stage phase transition process from a monoclinic (*C*2/*m*) to a trigonal ($P\bar{3}1m$) structure via the layer-by-layer slip mechanism under pressure. This transition is closely related to the interlayer interaction. To obtain a better understanding of the interlayer interaction, we calculated the total (Figure 1(b)) and projected electronic density of states (DOS) at 20 GPa for both bulk and monolayer $NiPS_3$ (Figure S2). It is shown that bulk $NiPS_3$ at 20 GPa exhibits a metallic behavior, whereas monolayer $NiPS_3$ shows a semiconducting behavior with a bandgap of 0.43 eV. These results suggest that the magnetic moments and electronic properties (metallic or semiconducting) are strongly correlated with the interlayer distance.

To confirm the calculated structure, we conducted high-pressure XRD measurements of $NiPS_3$. Figure 2(a) shows the diffraction patterns and their evolution with pressure.

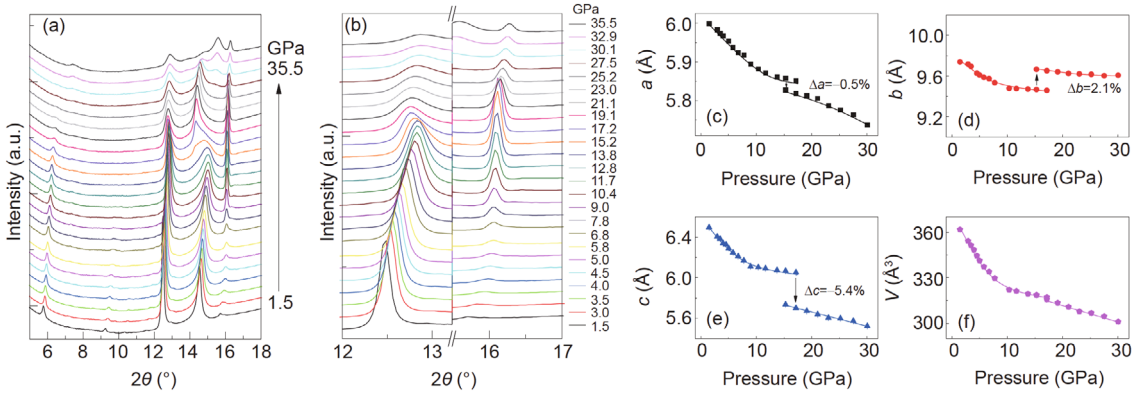

Figure 2 (Color online) *In situ* XRD patterns for the $NiPS_3$ powder sample. (a) Diffraction pattern of $NiPS_3$ and their evolution with pressure; the X-ray wavelength was λ = 0.6199 Å; (b) detailed information of the diffraction pattern of $NiPS_3$ from 12° to 17°; (c) experimental cell parameter *a* as a function of the applied pressure for the LP and HP phases of $NiPS_3$; (d) experimental cell parameter *b* as a function of the applied pressure for the LP and HP phases of $NiPS_3$; (e) experimental cell parameter *c* as a function of the applied pressure for the LP and HP phases of $NiPS_3$; (f) experimental cell volume (*V*) as a function of the applied pressure for the LP and HP phases of $NiPS_3$.

From the diffraction patterns, two distinct phase transitions can be observed at ~15 and 27 GPa. The first phase transition begins at ~15 GPa, and the transition is complete by ~20 GPa. The second phase transition occurs at ~27 GPa. At the first phase transition, a new diffraction peak develops, whereas another peak disappears. The evolution of the peak ~14.5° begins at ~15 GPa. It evolves into a new peak at ~20 GPa; the new phase is observed at this pressure. In addition to this change, the other two diffraction peaks at ~12.5° and ~16.0° (see Figure 2(b)) evolve ~15 GPa. Below 15 GPa, the peak ~12.5° gradually moves toward a higher angle as the pressure gradually increases, whereas, >15 GPa, it moves toward a lower angle first, and then continues to move toward a higher angle as the pressure increases. However, at < 15 GPa, the intensity of the peak ~16.0° increases with increasing pressure, whereas, >15 GPa, the intensity of this diffraction peak weakens with increasing pressure. Basing on the above phenomena, we believe that $NiPS_3$ undergoes the first phase transition at ~15 GPa. The phase transition at ~15 GPa has been verified by the Raman scattering measurement (see Figure S3). At the second phase transition, at ~27 GPa, new diffraction peaks develop while one peak disappears. The diffraction peak at ~6° disappears, and two new peaks appear at ~6.5° and 14.5° at ~27 GPa. Our experimental results are consistent with the calculated results shown in Figure 1(a).

To obtain a better understanding of the experimental data, we refined the powder XRD pattern using the Rietveld method [47] through the GSAS program (Figure S1). Almost all the diffraction peaks can be well indexed. Figure 2(c)-(f) show the refined lattice parameters *a*, *b*, *c*, and cell volume (*V*). From Figure 2(c)-(e), we can see that *a*, *b*, and *c* exhibit a consistent trend at <10 GPa. This interval corresponds to the LP phase. However, in the pressure range of 10-15 GPa, the variation of the unit cell parameters slows down with increasing pressure. This interval could be a transition interval. All unit cell parameters change suddenly above 15 GPa, and the volume gradually decreases with increasing pressure (Figure 2(f)). The lattice parameter *a* decreases by 0.5% (Figure 2(c)), *b* increases by 2.1% (Figure 2(d)), and *c* decreases by 5.4% (Figure 2(e)). Compared with the unit cell parameters *a* and *b*, the unit cell parameter *c*, which includes the vdW gap, decreases rapidly with pressure. This suggests that the effect of pressure on the interlayer interaction is significant. In this interval, a structural phase transition occurs, which corresponds to the transition to the HP-I phase. These HP-I and LP phases belong to the same space group of *C*2/*m*. For this reason, monoclinic unit cells with space group *C*2/*m* were adopted for cell parameter fitting for $NiPS_3$. However, because the XRD peaks at >30 GPa are weaker, fewer, and wider, they are difficult to fit. The fitting data above 30 GPa are therefore not given. Moreover, because 27-30 GPa belongs to the transition interval, in this interval we still use the HP-I structure for fitting. It can be found from the fitting results that the changes of the unit cell parameters are consistent with the results obtained through the simulation. The obvious decline of the interlayer distance provides favorable conditions for the 2D-3D crossover.

3.2 Insulator-metal transition

Infrared measurements have great utility in the understanding of the high-pressure electronic behavior of materials; for this reason, we performed infrared measurements on bulk $NiPS_3$ under high pressure. The high-pressure infrared measurement includes two parts: transmittance and reflectance. The transmittance of an insulator is close to 1, and the transmittance of a metal is close to 0. As can be seen from Figure 3(a), under ambient pressure, the transmittance of $NiPS_3$ is close to 1, thus indicating that at this pressure $NiPS_3$ is an insulator. As the pressure gradually increases, the transmittance of $NiPS_3$ gradually decreases, indicating that its bandgap is gradually decreasing, and the insulator gradually transitions to metal. When the pressure increases to 20.9 GPa, the transmittance of $NiPS_3$ is close to 0, and it therefore becomes a metal. Under further increases in pressure, the transmittance of $NiPS_3$ remains constant. Moreover, as the reflectance increases, the metallicity will increase; we thus observe further the metallization process through reflectance measurements. By observing the change of reflectance under varying pressures, we obtained confirmation of the above findings. From Figure 3(b), we can see that the reflectance is low, and the interference is high at 10 GPa. As the pressure gradually increases, the reflectance increases, and the spectrum gradually becomes smooth. At ~20.9 GPa, the spectrum is very smooth, suggesting that there is no interference between the top surface and the bottom surface of the $NiPS_3$ crystal, which is a typical characteristic of metallic behavior. The reflectance increases significantly when the pressure reaches to 24.4 GPa; above this value, the reflectance becomes stable. The signal at ~2000 cm^{-1} is the absorption signal of diamond. Moreover, we clearly observed the metallization process by optical reflection of $NiPS_3$ (for details, see Figure S4).

To verify the metallization behavior, we measured the resistance of bulk $NiPS_3$ under high pressure. Temperature-dependent resistances under different pressures are plotted in Figure 3(c)-(f). A transition from insulator to metal can be seen at ~20 GPa. From Figure 3(c)-(f), we can see that, as the pressure gradually increases, the resistance is gradually suppressed (for details, please see Figure S5). Figure 3(c)-(f) show the metallization process of $NiPS_3$. At 14.2 GPa, the data indicate the presence of an insulator; the data show an intermediate state at 17.2 GPa (Figure 3(c), (d)). With a further increase in pressure to ~20.2 GPa (Figure 3(e)), the sample is completely metalized. This good metallic behavior

is maintained at a pressure of 24.7 GPa (Figure 3(f)). This measurement confirms the result of the infrared measurements. The above measurement methods clearly confirm that the bulk $NiPS_3$ will undergo an insulator-metal phase transition under pressure. At present, related articles predict that monolayer MPX_3 will still maintain insulator or semiconductor behavior under high pressure without metallization [48]. Bulk $NiPS_3$ therefore exhibits 3D characteristics that are different from those of "pure" 2D (monolayer) $NiPS_3$. We speculate that the difference in behavior between bulk $NiPS_3$ and monolayer $NiPS_3$ may be caused by the interlayer interactions.

3.3 Magnetic properties

To confirm the correlation between the magnetic properties and the interlayer interaction of $NiPS_3$, we measured and calculated the magnetic properties of $NiPS_3$. By performing temperature-dependent Raman scattering measurements on bulk $NiPS_3$ at temperatures from 5.6 to 300 K at ambient pressure, we discovered a two-magnon signal of $NiPS_3$ centered at 550 cm^{-1}. Details can be seen in Figure S6. This finding is consistent with the results reported in other articles [49,50]. To investigate the effect of pressure on the two-magnon signal, we conducted Raman measurements of bulk $NiPS_3$ in the cross-polarization configuration under different pressures at the low temperature of 5 K (Figure 4(a)). In the cross-polarization configuration, some phonons, especially those superimposed on the two-magnon signal, are suppressed, such that the two-magnon signal in this configuration is clearer. From this data, we find that the two-magnon signal was gradually suppressed and shifted toward higher frequencies as the pressure increased. The two-magnon signal became very weak at ~22 GPa and was totally suppressed at ~27 GPa. Such behavior is reported for different polarization configurations and different temperatures. For

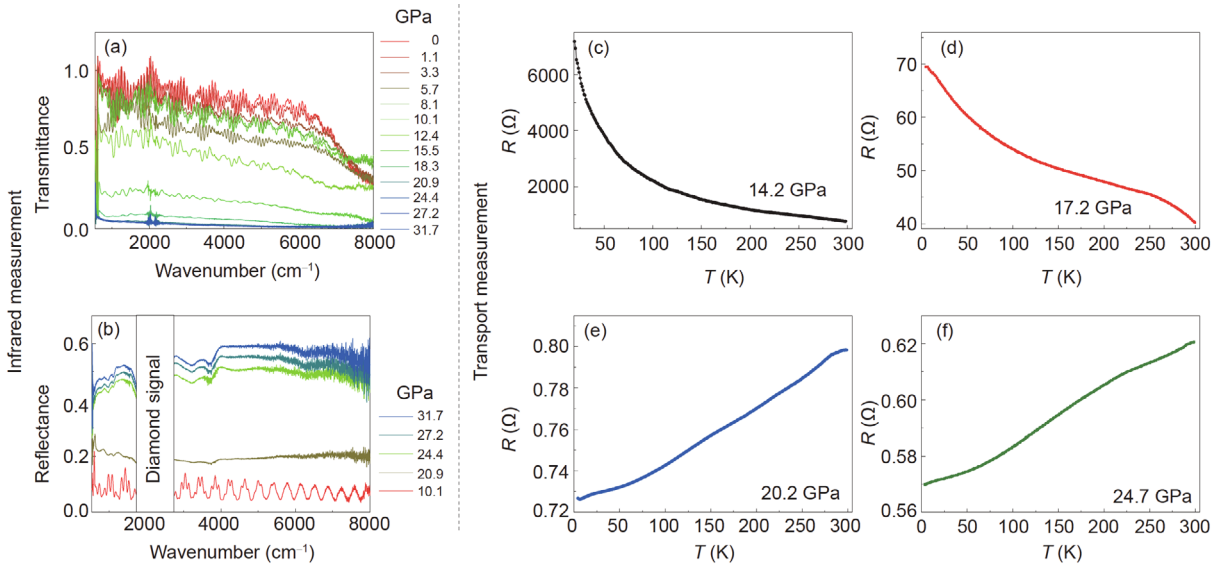

Figure 3 (Color online) Electronic behavior of the bulk $NiPS_3$ crystal under high pressure. (a), (b) Infrared measurement of bulk $NiPS_3$ under different pressures: transmittance (a) and reflectance (b). (c)-(f) Temperature-dependent resistance of $NiPS_3$ at pressures of 14.2, 17.2, 20.2, and 24.7 GPa, respectively. An insulator-metal transition can be observed at about 20 GPa.

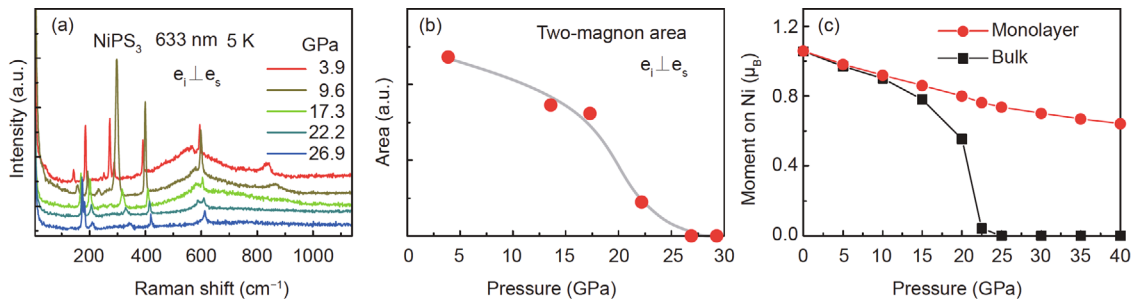

Figure 4 (Color online) Magnetic behavior of the $NiPS_3$ crystal under high pressure. (a) Raman spectra of bulk $NiPS_3$ in the cross-polarization configuration under different pressures at 5 K. (b) Two-magnon area of bulk $NiPS_3$ in the cross-polarization configuration under different pressures; the data points in (b) are extracted from the Raman spectra in (a). (c) Moment of $NiPS_3$ on Ni under different pressures.

details, see Figures S7 and S8. To quantitatively describe the change of magnetism with pressure, we fitted the data in Figure 4(a) and obtained the two-magnon area of bulk $NiPS_3$ under different pressures (Figure 4(b)). In Figure 4(b), we see that the area of the two-magnon signal decreases with increasing pressure. When the pressure reaches to ~27 GPa, the magnetism completely disappears.

In addition to experimental results, we calculated the magnetic moment of $NiPS_3$ under different pressures with an intralayer AFM structure [42]. In Figure 4(c), the calculated moments on the Ni sites are plotted as a function of the pressure up to 40 GPa for bulk $NiPS_3$. We see that the moments on the Ni sites decrease rapidly at 15 GPa and are quenched at ~22 GPa. This behavior is consistent with the trend of the two-magnon area changing with pressure in Figure 4(b). For comparison, we calculated the magnetic moments for monolayer $NiPS_3$ (just extend the interlayer spacing in a double cell along the *c*-axis) at each pressure. As shown in Figure 4(c), the moments on the Ni sites show an almost linear decrease with pressure and remain nonzero up to 40 GPa, indicating that the AFM state is expected to be stable in the monolayer limit under high pressure. Similar to the behavior of the electrical properties, the magnetic behavior of bulk $NiPS_3$ shows 3D characteristics that are different from those of "pure" 2D (monolayer) $NiPS_3$. These results suggest that the magnetic moments are strongly influenced by the interlayer interaction.

3.4 Phase diagram

Figure 5 shows the temperature-pressure phase diagram of bulk $NiPS_3$. The boundaries of the two structural phase transitions of $NiPS_3$ were determined via theoretical calculations and high-pressure XRD experiments and are indicated by two black dashed lines. Moreover, the boundary of the AFM-PM transition was obtained via Raman scattering experiments and theoretical calculations; this boundary is indicated by a blue dashed line. Through infrared and resistance measurements, as well as theoretical calculations, the insulator-metal transition of $NiPS_3$ occurs at ~20 GPa; this transition is indicated by a red dashed line in Figure 5. Two structural transitions are clearly visible at 15 and 27 GPa. The structure below 15 GPa is the LP phase. The phase in the range of 15-27 GPa is the HP-I phase, a transition region between the 2D and 3D behavior. The structure above 27 GPa is the HP-II phase. It can be seen from the phase diagram that the insulator-metal transition occurs in the intermediate phase (HP-I phase). The pink point in the figure is the resistance under different pressures at 300 K. As the pressure increases, the resistance suddenly decreases, and the sample metallizes at ~20 GPa. The AFM-PM transition occurs at the crossover between the HP-I and HP-II phases. As can be seen, the antiferromagnetic transition temperature

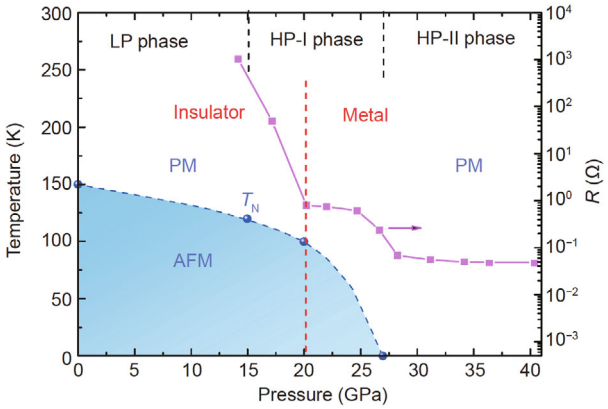

Figure 5 (Color online) Temperature-pressure phase diagram of bulk $NiPS_3$. The structural, magnetic, and electronic transitions are shown as a function of pressure. The pressures corresponding to the beginning and end of the gradual LP-HP-I-HP-II structural transition, the insulator-metal transition, and the AFM-PM transition are marked with black, red, and blue dashed lines, respectively. The pink points in the figure are the resistance under different pressures at 300 K. The blue points indicate the values of the antiferromagnetic transition temperature T_N under different pressures.

T_N is totally suppressed at 27 GPa; above this threshold, the AFM behavior disappears.

4 Conclusions

We reported the close correlation between the structural, electronic, and magnetic properties of $NiPS_3$ driven by external hydrostatic pressure. Dimensional crossover appears not just in structural phase transition but also in the electronic behavior and an evolution of the magnetic properties. Two new phases, namely, HP-I and HP-II, of $NiPS_3$ were proposed via *ab initio* calculations and confirmed through high-pressure XRD experiments. The change from the LP to the HP-I structure is accompanied by an $a/3$ slip along the *a*-axis. The space group of the material remains $C2/m$ across this transition, thus indicating an isostructural phase transition. Compared with the LP phase, the cell parameters change suddenly in the HP-I phase. In particular, the change in the interlayer distance is most obvious. As a result of these variations, the magnetism of bulk $NiPS_3$ is gradually suppressed, whereas the magnetism of monolayer $NiPS_3$ remains stable. Bulk $NiPS_3$ exhibits a transition from insulator to metal in this phase, whereas monolayer $NiPS_3$ remains a semiconductor under high pressure. The structural change from the HP-I to the HP-II phase is accompanied by an $a/2$ slip along the *a*-axis. In the meanwhile, a 2D-3D crossover occurs in the structure with a change of space group from $C2/m$ to $P\bar{3}1m$. Bulk $NiPS_3$ maintains metallic behavior in this phase. Due to the structural changes, the magnetism of bulk $NiPS_3$ is completely suppressed, and the magnetic moment on the Ni sites becomes zero. Both the electrical and magnetic properties show 3D characteristics that are differ-

ent from their "pure" 2D behavior under pressure. These results suggest that these properties are strongly correlated with the interlayer distance. The properties of this compound under pressure are nontrivial; as such, this material provides a good model for future research on the physical properties of other layered magnetic materials.

This work was supported by the National Key Research and Development Program of China (Grant Nos. 2016YFA0401503, 2018YFA0305700, 2017YFA0302904, 2020YFA0711502, and 2016YFA0300500), the National Natural Science Foundation of China (Grant Nos. 11575288, 11974387, U1932215, U1930401, 12004014, 22090041, and 11774419), the Strategic Priority Research Program and Key Research Program of Frontier Sciences of the Chinese Academy of Sciences (Grant Nos. XDB33000000, XDB25000000, and QYZDBSSW-SLH013), the Youth Innovation Promotion Association of Chinese Academy of Sciences (Grant No. Y202003), and the CAS Interdisciplinary Innovation Team (Grant No. JCTD-2019-01). ADXRD measurements were performed at 4W2 High Pressure Station, Beijing Synchrotron Radiation Facility (BSRF), which is supported by the Chinese Academy of Sciences (Grant Nos. KJCX2-SW-N20, and KJCX2-SW-N03). This work was partially carried out at high-pressure synergetic measurement station of synergetic extreme condition user facility.

Supporting Information

The supporting information is available online at http://phys.scichina.com and https://link.springer.com. The supporting materials are published as submitted, without typesetting or editing. The responsibility for scientific accuracy and content remains entirely with the authors.

1 A. K. Geim, and K. S. Novoselov, Nat. Mater. **6**, 183 (2007).
2 M. Chhowalla, H. S. Shin, G. Eda, L. J. Li, K. P. Loh, and H. Zhang, Nat. Chem. **5**, 263 (2013).
3 D. Jariwala, V. K. Sangwan, L. J. Lauhon, T. J. Marks, and M. C. Hersam, ACS Nano **8**, 1102 (2014).
4 S. Manzeli, D. Ovchinnikov, D. Pasquier, O. V. Yazyev, and A. Kis, Nat. Rev. Mater. **2**, 17033 (2017).
5 C. Gong, L. Li, Z. Li, H. Ji, A. Stern, Y. Xia, T. Cao, W. Bao, C. Wang, Y. Wang, Z. Q. Qiu, R. J. Cava, S. G. Louie, J. Xia, and X. Zhang, Nature **546**, 265 (2017), arXiv: 1703.05753.
6 J. U. Lee, S. Lee, J. H. Ryoo, S. Kang, T. Y. Kim, P. Kim, C. H. Park, J. G. Park, and H. Cheong, Nano Lett. **16**, 7433 (2016), arXiv: 1608.04169.
7 X. Li, and J. Yang, J. Mater. Chem. C **2**, 7071 (2014).
8 D. Lançon, H. C. Walker, E. Ressouche, B. Ouladdiaf, K. C. Rule, G. J. McIntyre, T. J. Hicks, H. M. Rønnow, and A. R. Wildes, Phys. Rev. B **94**, 214407 (2016).
9 A. R. Wildes, V. Simonet, E. Ressouche, G. J. McIntyre, M. Avdeev, E. Suard, S. A. J. Kimber, D. Lançon, G. Pepe, B. Moubaraki, and T. J. Hicks, Phys. Rev. B **92**, 224408 (2015).
10 A. R. Wildes, K. C. Rule, R. I. Bewley, M. Enderle, and T. J. Hicks, J. Phys.-Condens. Matter **24**, 416004 (2012).
11 A. R. Wildes, H. M. Rønnow, B. Roessli, M. J. Harris, and K. W. Godfrey, Phys. Rev. B **74**, 094422 (2006).
12 A. R. Wildes, B. Roessli, B. Lebech, and K. W. Godfrey, J. Phys.-Condens. Matter **10**, 6417 (1998).
13 A. R. Wildes, V. Simonet, E. Ressouche, R. Ballou, and G. J. McIntyre, J. Phys.-Condens. Matter **29**, 455801 (2017), arXiv: 1706.07989.
14 X. Li, X. Wu, and J. Yang, J. Am. Chem. Soc. **136**, 11065 (2014).
15 X. Li, T. Cao, Q. Niu, J. Shi, and J. Feng, Proc. Natl. Acad. Sci. USA **110**, 3738 (2013), arXiv: 1210.4623.
16 R. Brec, Solid State Ion. **22**, 3 (1986).
17 B. L. Chittari, Y. Park, D. Lee, M. Han, A. H. MacDonald, E. Hwang, and J. Jung, Phys. Rev. B **94**, 184428 (2016), arXiv: 1604.06445.
18 P. Rabu, and M. Drillon, Adv. Eng. Mater. **5**, 189 (2003).
19 F. Wang, T. A. Shifa, P. Yu, P. He, Y. Liu, F. Wang, Z. Wang, X. Zhan, X. Lou, F. Xia, and J. He, Adv. Funct. Mater. **28**, 1802151 (2018).
20 P. A. Joy, and S. Vasudevan, Phys. Rev. B **46**, 5425 (1992).
21 G. Ouvrard, R. Brec, and J. Rouxel, Mater. Res. Bull. **20**, 1181 (1985).
22 K. Du, X. Wang, Y. Liu, P. Hu, M. I. B. Utama, C. K. Gan, Q. Xiong, and C. Kloc, ACS Nano **10**, 1738 (2016).
23 C. T. Kuo, M. Neumann, K. Balamurugan, H. J. Park, S. Kang, H. W. Shiu, J. H. Kang, B. H. Hong, M. Han, T. W. Noh, and J. G. Park, Sci. Rep. **6**, 20904 (2016).
24 N. Kurita, and K. Nakao, J. Phys. Soc. Jpn. **58**, 232 (1989).
25 M. H. Whangbo, R. Brec, G. Ouvrard, and J. Rouxel, Inorg. Chem. **24**, 2459 (1985).
26 M. Piacentini, F. S. Khumalo, C. G. Olson, J. W. Anderegg, and D. W. Lynch, Chem. Phys. **65**, 289 (1982).
27 R. Brec, D. M. Schleich, G. Ouvrard, A. Louisy, and J. Rouxel, Inorg. Chem. **18**, 1814 (1979).
28 X. Fan, C. H. Chang, W. T. Zheng, J. L. Kuo, and D. J. Singh, J. Phys. Chem. C **119**, 10189 (2015).
29 M. Tsurubayashi, K. Kodama, M. Kano, K. Ishigaki, Y. Uwatoko, T. Watanabe, K. Takase, and Y. Takano, AIP Adv. **8**, 101307 (2018).
30 C. R. S. Haines, M. J. Coak, A. R. Wildes, G. I. Lampronti, C. Liu, P. Nahai-Williamson, H. Hamidov, D. Daisenberger, and S. S. Saxena, Phys. Rev. Lett. **121**, 266801 (2018).
31 Y. Wang, Z. Zhou, T. Wen, Y. Zhou, N. Li, F. Han, Y. Xiao, P. Chow, J. Sun, M. Pravica, A. L. Cornelius, W. Yang, and Y. Zhao, J. Am. Chem. Soc. **138**, 15751 (2016).
32 Y. Wang, J. Ying, Z. Zhou, J. Sun, T. Wen, Y. Zhou, N. Li, Q. Zhang, F. Han, Y. Xiao, P. Chow, W. Yang, V. V. Struzhkin, Y. Zhao, and H. K. Mao, Nat. Commun. **9**, 1914 (2018).
33 R. A. Evarestov, and A. Kuzmin, J. Comput. Chem. **41**, 1337 (2020).
34 H. S. Kim, K. Haule, and D. Vanderbilt, Phys. Rev. Lett. **123**, 236401 (2019), arXiv: 1808.09263.
35 M. J. Coak, S. Son, D. Daisenberger, H. Hamidov, C. R. S. Haines, P. L. Alireza, A. R. Wildes, C. Liu, S. S. Saxena, and J. G. Park, npj Quantum Mater. **4**, 38 (2019), arXiv: 1903.10971.
36 M. J. Coak, D. M. Jarvis, H. Hamidov, C. R. S. Haines, P. L. Alireza, C. Liu, S. Son, I. Hwang, G. I. Lampronti, D. Daisenberger, P. Nahai-Williamson, A. R. Wildes, S. S. Saxena, and J. G. Park, J. Phys.-Condens. Matter **32**, 124003 (2020).
37 X. Yu, F. Li, Y. Han, F. Hong, C. Jin, Z. He, and Q. Zhou, Chin. Phys. B **27**, 070701 (2018).
38 G. Kresse, and J. Furthmüller, Phys. Rev. B **54**, 11169 (1996).
39 P. E. Blöchl, Phys. Rev. B **50**, 17953 (1994).
40 J. P. Perdew, K. Burke, and M. Ernzerhof, Phys. Rev. Lett. **77**, 3865 (1996).
41 A. Tkatchenko, and M. Scheffler, Phys. Rev. Lett. **102**, 073005 (2009).
42 R. R. Rao, and A. K. Raychaudhuri, J. Phys. Chem. Solids **53**, 577 (1992).
43 J. T. Wang, C. F. Chen, and Y. Kawazoe, Phys. Rev. Lett. **106**, 075501 (2011).
44 J. T. Wang, C. F. Chen, H. Mizuseki, and Y. Kawazoe, Phys. Rev. Lett. **110**, 165503 (2013).
45 L. Zhao, C. Yi, C. T. Wang, Z. Chi, Y. Yin, X. Ma, J. Dai, P. Yang, B. Yue, J. Cheng, F. Hong, J. T. Wang, Y. Han, Y. Shi, and X. Yu, Phys. Rev. Lett. **126**, 155701 (2021), arXiv: 2102.00437.
46 W. Klingen, G. Eulenberger, and H. Hahn, Naturwissenschaften **55**, 229 (1968).
47 H. M. Rietveld, J. Appl. Crystallogr. **2**, 65 (1969).
48 H. Xiang, B. Xu, Y. Xia, J. Yin, and Z. Liu, RSC Adv. **6**, 89901 (2016).
49 S. S. Rosenblum, and R. Merlin, Phys. Rev. B **59**, 6317 (1999).
50 K. Kim, S. Y. Lim, J. U. Lee, S. Lee, T. Y. Kim, K. Park, G. S. Jeon, C. H. Park, J. G. Park, and H. Cheong, Nat. Commun. **10**, 345 (2019), arXiv: 1901.10890.